

ROTATION AND TURBULENCE OF THE HOT ICM IN GALAXY CLUSTERS

TAOTAO FANG¹, PHILIP HUMPHREY¹, AND DAVID BUOTE¹

(Received; Revised; Accepted)
 Draft version August 8, 2008

ABSTRACT

Cosmological simulations of galaxy clusters typically find that the weight of a cluster at a given radius is not balanced entirely by the thermal gas pressure of the hot ICM, with theoretical studies emphasizing the role of random turbulent motions to provide the necessary additional pressure support. Using a set of high-resolution, hydrodynamical simulations of galaxy clusters that include radiative cooling and star formation and are formed in a Cold Dark Matter universe, we find instead that in the most relaxed clusters rotational support exceeds that from random turbulent motions for radii, $0.1 - 0.5 r_{500}$, while at larger radii, out to $0.8 r_{500}$, they remain comparable. We also find the X-ray images of the ICM flatten prominently over a wide radial range, $0.1 - 0.4 r_{500}$. When compared to the average ellipticity profile of the observed X-ray images computed for 9 relaxed nearby clusters, we find that the observed clusters are much rounder than the relaxed CDM clusters within $\approx 0.4 r_{500}$. Moreover, while the observed clusters display an average ellipticity profile that does not vary significantly with radius, the ellipticity of the relaxed CDM clusters declines markedly with increasing radius, suggesting that the ICM of the observed clusters rotates less rapidly than that of the relaxed CDM clusters out to $\approx 0.6 r_{500}$. When these results are compared to those obtained from a simulation without radiative cooling, we find a cluster ellipticity profile in much better agreement with the observations, implying that over-cooling has a substantial impact on the gas dynamics and morphology out to larger radii than previously recognized. It also suggests that the 10%-20% systematic errors from non-thermal gas pressure support reported for simulated cluster masses, obtained from fitting simulated X-ray data over large radial ranges within r_{500} , may need to be revised downward. These results demonstrate the utility of X-ray ellipticity profiles as a probe of ICM rotation and over-cooling which should be used to constrain future cosmological cluster simulations.

Subject headings: galaxies: clusters: general — X-rays: galaxies: clusters — cosmology: theory — turbulence — methods: numerical

1. INTRODUCTION

Clusters of galaxies, the largest virialized structures in the universe, play a critical role in understanding the formation and evolution of large scale structure, and determining fundamental cosmological parameters. It is now well-known that the dark matter, the dominant component, makes up about 80% of the total gravitational mass of a typical galaxy cluster. The baryonic matter in galaxies accounts for about 3 — 5% of the total mass. The remaining mass is made up by hot gas distributed between galaxies, with temperatures over 10^7 K. This hot gas, called the “intracluster medium” (ICM), emits X-rays through thermal bremsstrahlung radiation, and makes galaxy clusters the second most luminous X-ray sources in the universe, after quasars. In the era of precision cosmology, it becomes imperative to measure accurately cluster properties, such as its gravitational mass, to a precision of a few percent.

The X-ray measurement of the density and temperature profiles of the hot ICM provides one of the most accurate methods to determine the cluster total gravitational mass. For clusters that have not been disturbed recently by a major merger, the hot ICM should obey hydrostatic equilibrium to a good approximation, representing a balance between the gravitational force and thermal gas pressure. For the special case of spherical symmetry the equation of hydrostatic equilibrium may be written,

$$\frac{dP_g}{dr} = -\rho_g \frac{GM(r)}{r^2}, \quad (1)$$

where ρ_g is the gas density, P_g is the thermal gas pressure, and

$M(r)$ is the mass enclosed within radius r . Applications of the X-ray method to constrain cosmological parameters include, e.g., measurements of the gas mass fraction (Allen et al. 2007, and references therein), virial mass function (e.g., Stanek et al. 2006, and references therein) and the relationship between the virial concentration and mass (Buote et al. 2007).

It is necessary to use cosmological hydrodynamical N-body simulations to test the key assumptions underlying equation [1]; i.e., spherical symmetry and negligible non-thermal pressure support of the hot ICM (e.g., Evrard et al. 1996; Thomas et al. 1998). Early studies showed that it is possible to recover the cluster mass within a factor of ~ 2 with X-ray telescopes such as *EINSTEIN* and *EXOSAT* (e.g., Tsai et al. 1994), where isothermal gas had to be assumed in the mock X-ray analysis. Most recent studies, which involve mock observations with the most advanced telescopes such as *Chandra*, allow the radial gas temperature profile to be measured, and use simulations that include a wider range of physical processes. They find that the global cluster mass, typically computed within a radius of fixed over-density (e.g., r_{500}), can be recovered more accurately, with systematic errors typically ranging from 5% to 20% (see, e.g., Nagai et al. 2007).

Over the past decade simulators have emphasized how much additional pressure support from random turbulent gas motion contributes to systematic errors in the X-ray method (e.g., Bryan & Norman 1998; Kay et al. 2004; Faltenbacher et al. 2005; Dolag et al. 2005; Rasia et al. 2006; Hallman et al. 2006; Vazza et al. 2006; Nagai et al. 2007; Brunetti & Lazarian 2007). It has also been noticed in such high-resolution, hydrodynamic simulations that while the velocity dispersion tensor of the ICM is approximately isotropic in

¹ Department of Physics & Astronomy, 4152 Frederick Reines Hall, University of California, Irvine, CA 92697; fangt@uci.edu

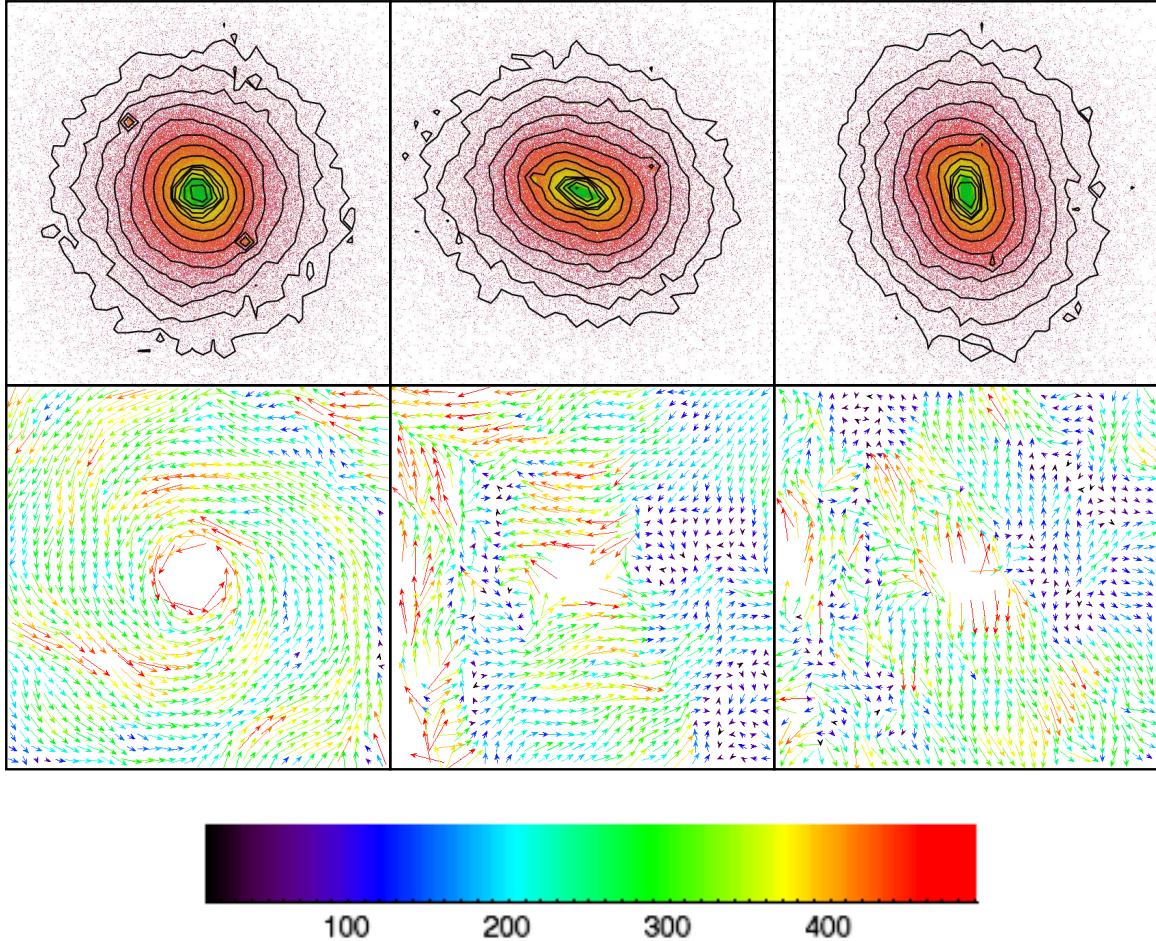


FIG. 1.— Top panel: mock *Chandra* X-ray flux maps of CL7 from x projection (left), y projection (middle), and z projection (right). Bottom panel: slice of the velocity field in the center of cluster CL7, y - z plane (left), x - z plane (middle), x - y plane (right). The bottom color bar is for the velocity field, and in units of km s^{-1} . Each box has a size of $1h^{-1} \times 1h^{-1} \text{ Mpc}^2$.

the outskirts of clusters, it becomes increasingly tangential at smaller radii, especially for the most relaxed systems (Rasia, Tormen, & Moscardini 2004; Lau et al. 2008, in preparation); Recently Lau et al. (2008) have shown the ICM velocity dispersion becomes increasingly tangentially anisotropic as one moves inward from r_{500} , such that for their relaxed clusters the anisotropy parameter falls to $\beta \approx -0.3$ near $0.2r_{500}$. These authors consider the non-thermal pressure support of this random turbulent motion (both radial and tangential) on estimates of M_{500} assuming hydrostatic equilibrium. However, rotational support of the gas, and its observable signatures, is not addressed.

In this paper, we show that for the relaxed clusters studied by Lau et al. (2008; Nagai et al. 2007) support of the ICM from rotational and streaming motions is comparable to the support from the random turbulent pressure out to $\approx 0.8r_{500}$. While the overall magnitude of the rotational motion (\sim a few hundred km s^{-1}) is not large enough to be detected directly through Doppler shifts of emission lines in X-ray spectra, even with the most advanced X-ray telescopes we have today (e.g., Sunyaev et al. 2003; Inogamov & Sunyaev 2003; Schuecker et al. 2004; Brüggen et al. 2005; Pawl et al. 2005; Chepurnov & Lazarian 2006; but see Dupke & Bregman 2006 for a recent measurement), simulated clusters with large-scale rotation are significantly flat, and this translates to observable large ellipticities of the X-ray isophotes. By com-

paring the ellipticities of the X-ray isophotes of the relaxed simulated clusters to those of nine observed clusters, we show that the observed clusters are, on average, much rounder and have a distinctly different radial variation in ellipticity. This demonstrates the utility of X-ray ellipticity profiles as a constraint for future cosmological cluster simulations.

This paper is organized as follows. In §2 we study the importance of ICM rotation in the 16 simulated clusters of Lau et al. (2008; Nagai et al. 2007), focusing our discussion using the examples of one relaxed and one disturbed cluster. In §3 we present ellipticity profiles of nine clusters obtained from X-ray observations with *Chandra* and *ROSAT* and compare them to the simulated clusters. The last section is devoted to summary and discussion.

2. NON-THERMAL GAS MOTION IN THE SIMULATED CLUSTERS

2.1. Simulation Data

We use a set of 16 high-resolution, cosmological hydrodynamic simulations of cluster-sized systems in a flat ΛCDM model: $\Omega_m = 0.3$, $\Omega_\Lambda = 0.7$, $\Omega_b = 0.043$ and $\sigma_8 = 0.9$ (the power spectrum normalization at $8h^{-1} \text{ Mpc}$ scale). These cluster-sized simulations include collisionless dynamics of dark matter, star and intracluster gas. They also include several critical physical processes such as radiative cooling, star formation and metal enrichment (CSF simulation). For comparison we also analyze one adiabatic cluster simulation, i.e., no radiative

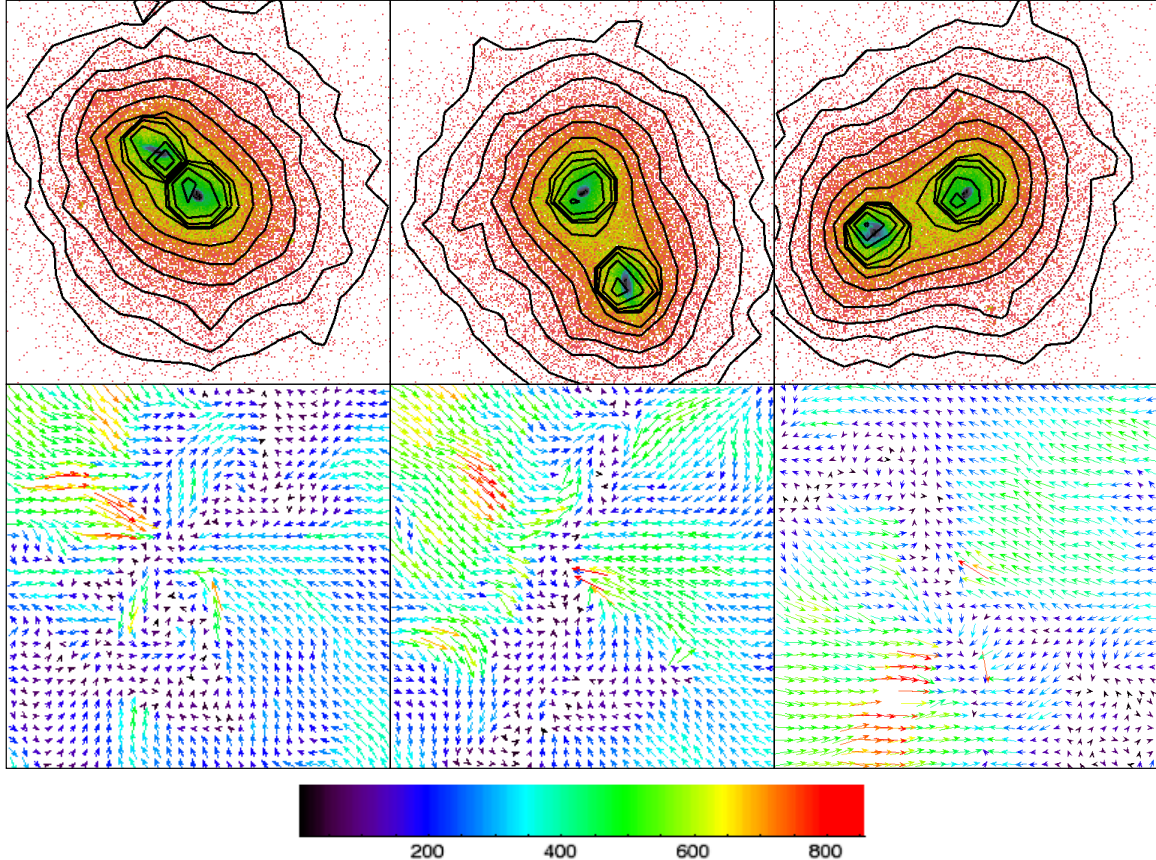


FIG. 2.— Top panel: mock *Chandra* X-ray flux maps of CL11 from x projection (left), y projection (middle), and z projection (right). Bottom panel: slice of the velocity field in the center of cluster CL11, y - z plane (left), x - z plane (middle), x - y plane (right). The bottom color bar is for the velocity field, and in units of km s^{-1} . Each box has a size of $1h^{-1} \times 1h^{-1} \text{ Mpc}^2$.

cooling and star formation (NC simulation). We refer readers to Nagai et al. (2007) for details, and provide a brief summary here. We adopt a Hubble constant of $H_0 = 100h \text{ km s}^{-1} \text{ Mpc}^{-1}$ where $h = 0.7$ throughout the paper.

The simulations use the Adaptive Refinement Tree (ART) N-body + gasdynamics code (Klypin et al. 2001; Kravtsov et al. 2002, 2006; Nagai et al. 2007), and run in two computational boxes: $120h^{-1} \text{ Mpc}$ for CL101–107, and $80h^{-1} \text{ Mpc}$ for the rest. The ART is a shock-capturing code that is particularly suited for capturing shocks and turbulent motion, and the use of adaptive mesh refinement also allows us to resolve the detailed cluster structure and the internal gas flows in clusters. These simulations achieve a dynamic range of $\sim 5 \times 10^{13} - 10^{15} h^{-1} M_\odot$, and a peak resolution of $\sim 6h^{-1} \text{ kpc}$, which is well-matched to the spatial resolution of *Chandra* X-ray observations of nearby galaxy clusters. Table 1 of Nagai et al. 2007 shows the typical properties of simulated clusters, all the parameters are computed from simulations within a region with an over-density of 500, with respect to the critical density of the universe. These clusters have masses ranging between $\sim 3 \times 10^{13} h^{-1} M_\odot$ and $10^{15} h^{-1} M_\odot$, and temperatures between 1 keV and 8.7 keV.

The simulated clusters are projected along three orthogonal directions x, y, z , and X-ray flux maps are created for each projection. (These coordinate axes reflect the orientation of the entire simulation box and are not adjusted to match the principle axes of each cluster.) We make the mock *Chandra* images by convolving the emission spectrum with the response of the *Chandra* front-illuminated CCDs and with an exposure of 100

ksec, a typical exposure for *Chandra* observations. We show the images and velocity structures of a relaxed cluster (CL7) in Figure 1 and a disturbed cluster (CL11) in Figure 2. CL7 is judged to be the most relaxed cluster in the simulation sample, with a gravitational mass of $M_{500} = 2.01 \times 10^{14} M_\odot$ and a size of $r_{500} = 0.891 \text{ kpc}$. Here r_{500} is defined as a radius of 500 times the mean density of the universe, M_{500} is the total gravitational mass within r_{500} . In contrast, CL11 is a very disturbed system with $M_{500} = 1.29 \times 10^{14} M_\odot$ and $r_{500} = 0.767 \text{ kpc}$.

The top panel of Figure 1 shows the projected X-ray emission maps of CL7, in the three orthogonal directions x, y, z from left to right, respectively. The X-ray contours (solid lines) are separated by a factor of ~ 2 in surface brightness, with the highest contour at a level of ~ 500 photons per pixel. The box size of the image is $1 h^{-1} \text{ Mpc}$. The cluster has a very regular appearance in all projections. However, the X-ray isophotes display significant elongation in the y and z projections compared to the much rounder isophotes of the x projection.

The bottom panel of the Figure 1 shows the two dimensional velocity field in the central slices of the simulated cluster CL7. The left plot is along the y - z plane, the middle plot is along the x - z plane, and the right is the x - y plane. The velocity vector is color-coded between 0 and 500 km s^{-1} , with the magnitude showing in the bottom color bar. The most striking feature is that while in both x - z and x - y planes the gas is moving largely randomly, in y - z plane the gas shows a very regular, counterclockwise, rotational motion with veloc-

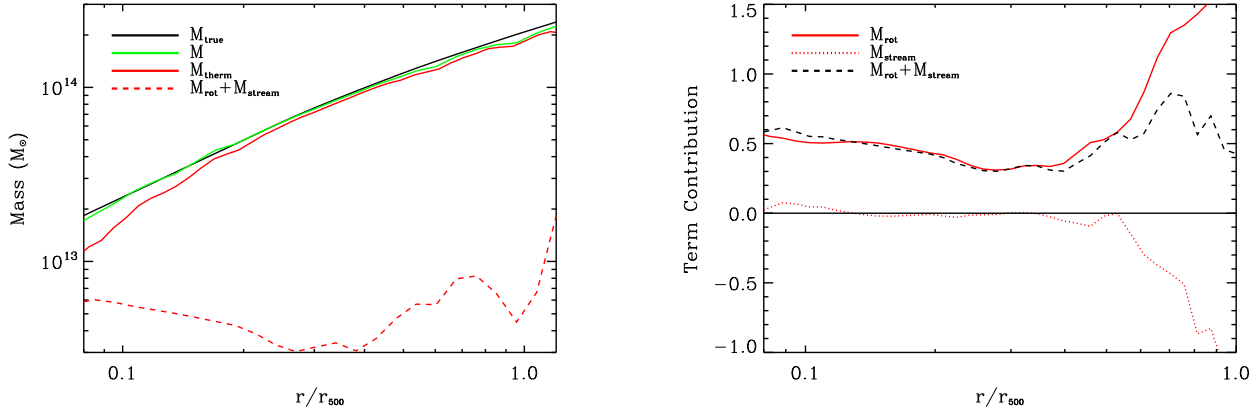


FIG. 3.— (Left Panel) Mass profiles of the relaxed simulated cluster CL7. The “true” mass M obtained by directly counting the masses of the gas and dark matter particles from the simulations is given by the dark solid line. The other lines represent the different mass components obtained by substituting Euler’s equation into Gauss’s Law (see §2.2): the component from thermal gas pressure, M_{therm} (red solid line), rotation and streaming motion, $M_{\text{rot}} + M_{\text{stream}}$ (red dashed line), and their sum, $M_{\text{therm}} + M_{\text{rot}} + M_{\text{stream}}$ (green solid line). (Right Panel) Separate contributions of M_{rot} (red solid line) and M_{stream} (red dotted line) to the mass profile, in units of $10^{13} M_{\odot}$. The dashed black line is the total contribution, $M_{\text{rot}} + M_{\text{stream}}$.

ities between 200–400 km s^{−1}.

In contrast, CL11 is a merging cluster with violent gas motion (Figure 2). Merging in the central region creates large scale gas motions on the order of 1,000 km s^{−1}. Such merging activity is clearly visible in the velocity fields shown in the y – z plane and x – z plane: gas is moving from the north-west and south-east directions toward the center. The X-ray images in the three projections are also distorted. Unlike CL7 ordered rotational motion is unimportant in all projections.

In the following subsections we compare the contribution of rotation (and other streaming motion) to that of random turbulent motion in supporting the weight of the ICM of the simulated clusters.

2.2. Analysis Method

The total cluster mass (M) enclosed within a surface \mathbf{S} is given by Gauss’s Law,

$$M = \frac{1}{4\pi G} \int \nabla \Phi \cdot d^2\mathbf{S}, \quad (2)$$

where Φ is the gravitational potential and G is the gravitational constant. Assuming the ICM is a steady state, inviscid, collisional fluid we may use Euler’s equation to eliminate Φ in favor of the gas pressure and terms involving the velocity components of the ICM,

$$M = \frac{1}{4\pi G} \int \left[-\frac{1}{\rho_g} \nabla P_g - (\mathbf{v} \cdot \nabla) \mathbf{v} \right] \cdot d^2\mathbf{S},$$

where ρ_g is the gas density and P_g represents the pressure arising from gas motions having a random (i.e., Maxwellian) velocity distribution.

We rewrite the previous equation as a sum of four terms,

$$M = M_{\text{therm}} + M_{\text{turb}} + M_{\text{rot}} + M_{\text{stream}}. \quad (3)$$

The first two terms on the r.h.s.,

$$M_{\text{therm}} = -\frac{1}{4\pi G} \int \left(\frac{1}{\rho_g} \nabla P_{\text{therm}} \right) \cdot d^2\mathbf{S} \quad (4)$$

$$M_{\text{turb}} = -\frac{1}{4\pi G} \int \left(\frac{1}{\rho_g} \nabla P_{\text{turb}} \right) \cdot d^2\mathbf{S}, \quad (5)$$

represent pressure support from random gas motions. Here $P_{\text{therm}} = kT/\mu m_p$ is the thermal gas pressure, where k is the Boltzmann constant, T is temperature, m_p is the proton mass, and μ is the atomic weight. The quantity P_{turb} is the pressure from random turbulent motions. The last two terms on the r.h.s.,

$$M_{\text{rot}} = \frac{1}{4\pi G} \int \left(\frac{v_\theta^2 + v_\phi^2}{r} \right) \cdot d^2\mathbf{S} \quad (6)$$

$$M_{\text{stream}} = -\frac{1}{4\pi G} \int \left(v_r \frac{\partial v_r}{\partial r} + \frac{v_\theta}{r} \frac{\partial v_r}{\partial \theta} + \frac{v_\phi}{r \sin \theta} \frac{\partial v_r}{\partial \phi} \right) \cdot d^2\mathbf{S} \quad (7)$$

follow by evaluating $(\mathbf{v} \cdot \nabla) \mathbf{v}$ in spherical coordinates (Binney & Tremaine 1987). Here M_{rot} is the contribution from rotational motion while M_{stream} includes the contributions from other streaming motion.

The combination $M_{\text{rot}} + M_{\text{stream}}$ represents the total contribution to the gravitational support from non-random gas motions. In this paper we are especially concerned with assessing the relative importance of non-random gas motions to that of the random turbulent motion. However, we also find it useful to separate the non-random contribution into the terms M_{rot} and M_{stream} . For a cluster supported mostly by rotation M_{rot} will dominate M_{stream} . For a non-rotating cluster with substantial non-random motions, M_{rot} and M_{stream} will be of similar magnitude (but will not necessarily cancel). Hence, in our discussion below we always consider the total $M_{\text{rot}} + M_{\text{stream}}$ when assessing the relevance of non-random gas motions, but we use M_{rot} ($\gg M_{\text{stream}}$) as a rotation proxy particularly for the relaxed clusters.

In what follows we choose the surface \mathbf{S} to be that of a sphere, but we emphasize that we do not assume the cluster is spherical and use the full three-dimensional ICM properties produced by the simulation to evaluate the integrals. Furthermore, we do not explicitly calculate M_{turb} since it depends critically on the sizes, velocities, temperatures, and densities of the coherent clumps that move randomly within the ICM. Instead, we infer its magnitude from $M_{\text{turb}} = M - M_{\text{therm}} - M_{\text{rot}} - M_{\text{stream}}$, where M is the total “true” mass of the gas and dark matter computed directly from the particles in the simulation.

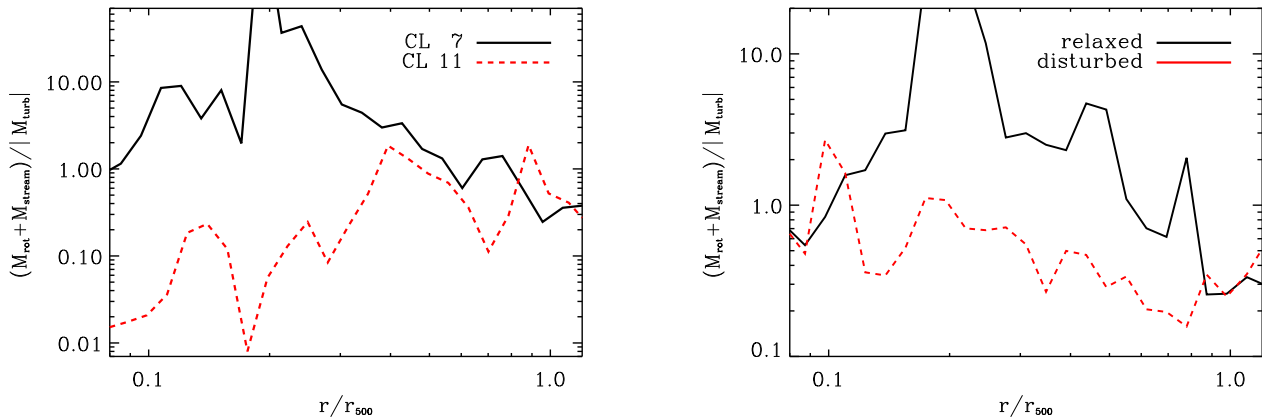


FIG. 4.— (Left Panel) Relative contribution of rotation and other streaming motion to the (absolute value of the) turbulent motion in CL7 (solid black line) and CL11 (dashed red line). (Right Panel) The same quantity is plotted by averaging the results for all of the seven relaxed clusters (solid black line) and all of the nine disturbed clusters (dashed red line) in the simulation.

To compute the mass profile associated with both the “true” mass and the mass components based on Eq.[4–7], we make use of the grid data that is generated from the raw data of the adaptive mesh refinement simulation. Specifically, the raw data is interpolated onto a uniform 256^3 cube grid in a $2h^{-1} \times 2h^{-1} \times 2h^{-1}$ Mpc³ box, centered on the simulated cluster. The spatial resolution therefore is $7.8h^{-1}$ kpc.

We divide the simulation box into a number of radial bins, and compute each mass component. At each radial bin, the entire surface is divided into small cells along θ and ϕ directions, over which the integration is performed. Specifically, in each cell we throw test particles randomly, we then compute the mean density, thermal pressure, and velocity by averaging all the test particles. Again, since we use Gauss’s Law and compute the integration in three dimensions, our analysis is entirely general with regard to the cluster geometry.

2.3. Mass Profiles

In the left panel of Figure 3 we show the “true” mass profile of the relaxed cluster CL7 obtained by directly counting the dark matter and mass particles from the simulation. Also displayed are various combinations of M_{therm} , M_{rot} , and M_{stream} , that result from substituting Euler’s equation into Gauss’s Law as discussed in the previous section. We consider seriously the gas properties of the simulated clusters down to a radius of $\approx 0.08r_{500}$. Below this radius the well-known effect of over-cooling produces unphysical gas density and temperature profiles.

Over most of the cluster region displayed, M_{therm} systematically underestimates the “true” mass by 5%-10%. Rotational and other streaming motions provide most of the non-thermal support of the cluster weight over a large range of radii. The combination of $M_{\text{therm}} + M_{\text{rot}} + M_{\text{stream}}$ (green solid line in the Figure 3) is within a few percent of the “true” mass out to $\approx 0.5r_{500}$. For these radii, $M_{\text{rot}} \gg M_{\text{stream}}$ (see right panel of Figure 3), indicating that rotation is the most important streaming motion, consistent with the visual impression of the velocity field shown in Figure 1.

We provide a direct comparison of rotation and streaming motions to random turbulent motions in Figure 4. (Note we take the absolute value of M_{turb} since it fluctuates about zero when its magnitude is small.) Over approximately

$0.1 - 0.5r_{500}$, $M_{\text{rot}} + M_{\text{stream}}$ generally dominates M_{turb} and remains comparable to M_{turb} all the way out to $\approx 0.8r_{500}$. Since, as noted above, $M_{\text{rot}} \gg M_{\text{stream}}$ within $\approx 0.5r_{500}$, it follows that M_{rot} dominates the non-thermal support of the cluster weight in that region.

In contrast, for the disturbed cluster CL11 $M_{\text{turb}} \gtrsim M_{\text{rot}} + M_{\text{stream}}$ over all radii shown (Figures 3 and 4). Rotational motion does not dominate, consistent with the lack of circular motion noted from visual inspection of the velocity field shown in Figure 2. Despite the differences between CL7 and CL11, it is interesting to note that for CL11 M_{therm} typically lies within $\pm 10\%$ of the “true” mass. This is of similar magnitude to CL7, except that CL7 only underestimates the “true” mass.

The basic results for CL7 and CL11 apply generally to the other relaxed and disturbed clusters in the simulation. In particular, we show in the right panel of Figure 4 the relative contribution of rotation and other streaming motion to the turbulent motion by averaging the results for all of the relaxed clusters (solid black line) and all of the disturbed clusters (dashed red line) in the simulation. (We have used the same clusters designated as “relaxed” or “disturbed” as Nagai et al. 2007). While there is substantial scatter (not shown) about these average profiles, particularly for the disturbed systems, $M_{\text{rot}} + M_{\text{stream}}$ generally dominates M_{turb} over approximately $0.1 - 0.5r_{500}$ and remains comparable to M_{turb} all the way out to $\approx 0.8r_{500}$. In the disturbed clusters, M_{turb} exceeds the rotational and streaming terms over most of the region within r_{500} .

2.4. Adiabatic Simulation

We also analyze a simulation that starts from the same initial conditions as those adopted in CL7. However, in this simulation, the ICM of the cluster – called “CL7a” – evolves adiabatically, i.e., without radiative cooling. The major difference between these two sets of simulations is that the CSF clusters suffer the so-called “over-cooling” problem (e.g., Balogh et al. 2001): cooling can produce a substantial amount of cold gas that is likely a few times higher than what are observed in real clusters (Gnedin et al. 2004).

In the left panel of Figure 6 we plot mass profiles for various terms in CL7a, applying the same method that we used

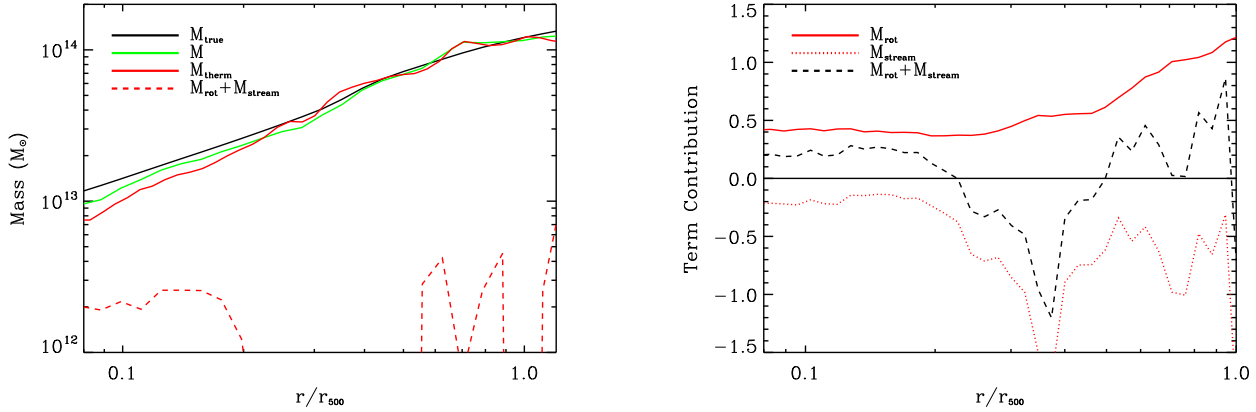


FIG. 5.— Same as Figure 3 but for the disturbed simulated cluster CL11.

for CL7. For this simulation unfortunately part of the temperature data is corrupted, and we have only those within $1h^{-1}$ Mpc box and compute the mass profiles out to $\sim 0.6 r_{500}$. Clearly, for the simulation without radiative cooling, M_{therm} closely follows the total mass, and the contribution from $(M_{\text{rot}} + M_{\text{stream}})$ is less than 5% over most radii. This is in sharp contrast to the case of CL7, in which the contribution from the $(M_{\text{rot}} + M_{\text{stream}})$ can be up to 10 – 20%, especially in the inner regions (see left panel of Figure 3). This suggests that rotation and streaming motion contribute less to the gas dynamics in the NC simulations; i.e., that without radiative cooling.

To illustrate the different between the CSF and NC simulations, we also plot the rotational velocities in the CL7 and CL7a. The right panel of Figure 6 shows the rotational velocity as a function of radius. We take the equatorial plane and average the gas velocity projection in the plane in each radial bin. We notice that both NC and CSF simulations show similar gas velocities at $\gtrsim 0.3r_{500}$, between 200 and 300 km s^{-1} . However, at the inner regions, the gas velocity in the CSF simulation rises sharply to above 1000 km s^{-1} , while the NC simulation shows a steady decline.

The substantial gas rotation has a strong impact on the gas dynamics in the central regions. This can be quantified by the ratio (R_E) between the kinetic energy in rotation (KE_{rot}) and the thermal energy (E_{therm}). For the CSF cluster CL7, we have

$$R_E \equiv \frac{KE_{\text{rot}}}{KE_{\text{therm}}} = \frac{(1/2)\rho_g v_{\text{rot}}^2}{(3/2)n_g k_B T_g} \quad (8)$$

$$= 0.23(v_{\text{rot}}/600 \text{ km s}^{-1})^2 (T_g/3.5 \text{ keV})^{-1}, \quad (9)$$

where v_{rot} is the rotation velocity. Taking the typical rotational velocity of $\sim 600 \text{ km s}^{-1}$ at $\sim 0.1r_{500}$ in CL7 (see Figure 6), we estimate the rotational kinetic energy can be as high as about 23% of the thermal energy. This is actually a conservative lower limit since the gas temperature peaks at $\sim 3.5 \text{ keV}$ (Nagai et al. 2007). It can be as low as $\sim 1 \text{ keV}$ in the innermost regions. This ratio decreases to about 10% between 0.2 and 0.3 r_{500} . However, for CL7a, due to the relative low velocity, this ratio stays below 10% at most radii. In fact, in the adiabatic simulation the R_E value at 0.1 r_{500} is only about 1/10 the value obtained for the simulation with cooling and star formation.

3. ICM ROTATION AND ELLIPTICITY

3.1. Motivation

The substantial ICM rotation predicted by the simulations for relaxed CDM clusters needs to be tested by observations. The straightforward approach to detect rotation and other bulk motion of the ICM in clusters is to measure Doppler shifts and broadening of emission lines in their X-ray spectra. For a typical bulk-motion velocity of $\sim 500 \text{ km s}^{-1}$, Sunyaev, Norman & Bryan (2003) estimated that the Doppler shift of an iron line at 6.7 keV would be $\sim 10 \text{ eV}$. The X-ray Spectrometer (XRS) on Astro-E2 would have been the first instrument to perform such measurements for many clusters. But its failure soon after launch means we must await the next generation of X-ray satellites, such as *Constellation-X*, *XEUS* and *Spectrum-X*, for direct measurements of ICM motions in many clusters.

In the classic cooling flow model, gas rotation is expected near the center of the flow due to mass and angular momentum conservation (e.g., Mathews & Brighenti 2003). In the case of elliptical galaxies, the X-ray images are expected to be considerably flattened toward the equatorial plane (e.g., Brighenti & Mathews 1996; Mathews & Brighenti 2003). X-ray morphological information, such as ellipticity, can be used to probe this process then. X-ray studies that assume negligible ICM rotation indicate that both the radial profile (e.g., Pratt & Arnaud 2003; Lewis, Buote, & Stocke 2003; Vikhlinin et al. 2006; Gastaldello et al. 2007) and ellipticity (Buote & Canizares 1996) of the gravitating mass of nearby clusters agree with the radial profile and ellipticity of the dark matter of simulated CDM clusters. Therefore, if the ICM of the simulated CDM clusters in our study is flattened substantially by rotation, their X-ray images on average should have larger ellipticities than observed clusters.

Since X-ray ellipticity can be measured precisely for many clusters, below we compare results for the simulated CDM clusters to a sample of observed clusters. We will also compare to a simulated CDM clusters that involves no radiative cooling and star formation. This comparison will help us understand the role of over-cooling. We note that previous studies found that the simulation we use here reproduces reasonably well the spherically averaged global ICM properties of observed clusters (Nagai et al. 2007; Kravtsov et al. 2006).

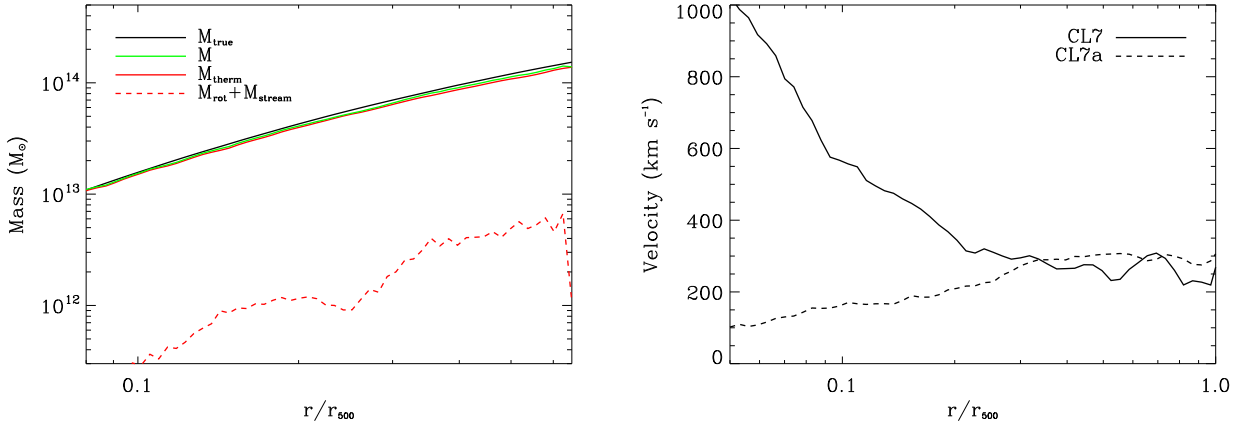


FIG. 6.— Left panel: same as the left panel of Figure 3 but for CL7a. Right panel: rotational velocity as a function of radius for CL7 (solid line) and CL7a (dashed line).

3.2. Ellipticity of Relaxed CDM Clusters

We begin by computing the ellipticity profiles of the X-ray images of the relaxed simulated cluster CL7 for the three orthogonal projections shown in Figure 1. The iterative moment-based procedure we use to evaluate the ellipticities of the simulated X-ray images is the same as that discussed below for the observations of real clusters (§3.4.4). We show the X-ray ellipticity profiles for CL7 in Figure 7.

The X-ray ellipticities of the x -projection are small and have a nearly constant value (≈ 0.10) from $0.1 - 0.7 r_{500}$ eventually falling to (≈ 0.05) at r_{500} . The very round X-ray isophotes are expected in this projection since one is essentially looking down the axis of rotation. In contrast, the ellipticities are much larger and show a much stronger variation with radius in the other two projections. For the y -projection, the ellipticity is $0.6 - 0.7$ between radii $0.1 - 0.2 r_{500}$, declines to ≈ 0.5 at $0.3 r_{500}$, and continues to fall with radius until reaching a value of ≈ 0.25 at r_{500} . The z -projection has ellipticities similar to the y -projection but with $\approx 10\%$ smaller values for most radii.

The X-ray ellipticities for radii $0.1 - 0.3 r_{500}$ in the y and z projections are considerably larger than those of the dark matter (≈ 0.4), which also decline with increasing radius. The larger X-ray ellipticities with respect to the dark matter imply substantial rotational flattening of ICM, because (1) the gravitational potential of an ellipsoid is never flatter than the mass distribution that generates it, (2) for (non-rotating) single-phase hot gas in hydrostatic equilibrium, the X-ray emissivity has the same shape as the gravitational potential, independent of the temperature profile of the gas (“X-Ray Shape Theorem”, Buote & Canizares 1994, 1998), and (3) M_{rot} dominates M_{stream} and M_{turb} .

As a consistency check, we note that at $0.1 r_{500}$ both M_{rot}/M_{therm} and R_E (section 2.4) are about 0.25 for CL7, indicating substantial rotational support. Moreover, $1 + R_E \sim 1.25$ provides an approximate indication of the axial ratio induced by rotation, and this can explain most of the excess X-ray ellipticity over that produced by the flattened dark matter potential.

To make a proper comparison of the X-ray ellipticity profile of the simulated CDM clusters to the average ellipticity profile of observed clusters we average the ellipticity profiles of CL7 obtained by viewing 100 projections of random ori-

entation (θ, ϕ). The average ellipticity profile is calculated by averaging all the ellipticity values of a particular radius obtained for the 100 simulations. To achieve fast computation, we approximate the X-ray emissivity in each cell as $\propto n_g^2 T^{1/2}$, appropriate for thermal bremsstrahlung radiation. We verified this approximation by comparing to the profiles for the three orthogonal projections computed using the full expression for the plasma emissivity.

The angle-averaged X-ray ellipticity profile for CL7 is shown in Figure 7. The average profile is similar to that from the y and z projections but with somewhat smaller values; i.e., the ellipticity declines from ≈ 0.6 at $0.1 r_{500}$ to ≈ 0.3 at $0.3 r_{500}$ and then settles to a value between 0.15-0.20 at larger radii.

Using the same procedure, we computed average ellipticity profiles for the other “relaxed” clusters in the simulation. Since below we consider observations of clusters (rather than lower mass groups), we only include the relaxed simulated clusters with masses above $10^{14} h^{-1} M_\odot$; i.e., CL3, CL5, CL7, and CL104. We angle-averaged the profiles of these systems and plot the combined average profile of these four systems in Figure 8. The combined profile is very similar to that of CL7 (Figure 7).

3.3. Comparison to Adiabatic Simulation

For comparison, in Figure 7 (dark dashed line) we show the average ellipticity profile of CL7a obtained from the simulation without cooling or star formation (NC). Since we don’t have the temperature data outside of the $1 h^{-1}$ Mpc box and the X-ray emissivity has a very weak dependency on temperature, we approximate the X-ray emissivity in each cell as $\propto n_g^2$. We test our results within the $1 h^{-1}$ Mpc box and do not find any major difference between these two approximations. Within the central regions ($\sim 0.25 r_{500}$) the ellipticity of the NC cluster is considerably smaller compared to the CSF simulation. In fact, the ellipticity profile remains nearly constant with a value ~ 0.25 for radii larger than $0.1 r_{500}$. The much smaller ellipticity in CL7a is consistent with the much smaller rotational support compared to CL7. From Figure 6 one can see that the very different gas velocities near $0.1 r_{500}$ translate to R_E values in CL7a a factor of 10 smaller than in CL7. At $0.3 r_{500}$, the gas velocities of CL7 and CL7a are similar, as are their average X-ray ellipticities. The slightly smaller ellipticity values of CL7 at larger radii reflect both the

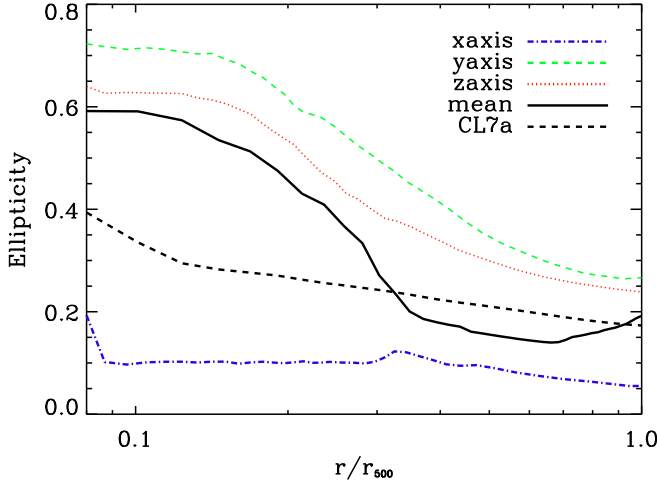


FIG. 7.— X-ray ellipticity profiles of the simulated cluster CL7 obtained by projecting the cluster along the x -axis (blue), y -axis (green), and z -axis (red). The dark solid line is the mean profile obtained by averaging the profiles from 100 projections of random orientation (see text), and the dark dashed line is the mean profile of the cluster in the simulation without radiative cooling and star formation.

slightly smaller gas velocities over that range (see Figure 6) and the fact that CL7 is slightly more centrally concentrated than CL7a. Clearly, the gas dynamics and morphology differ substantially, particularly within $\sim 0.3r_{500}$, depending on whether cooling is included in the simulations.

3.4. Ellipticity of Observed Clusters

3.4.1. Sample definition

In order to effect a comparison between the observable properties of the simulated clusters and real data, we selected a sample of nearby *relaxed* clusters observed with the *ROSAT* PSPC and with *Chandra*. We opted to use these complementary satellites since the large, unobstructed field of view ($\sim 20'$ radius) makes *ROSAT* ideal for the unbiased computation of ellipticities out to radii in excess of ~ 500 kpc for most interesting systems. Its modest spatial resolution ($0.5'$ FWHM at 1 keV; corresponding to ~ 50 kpc at $z=0.1$) of the PSPC will not significantly bias the ellipticity calculation within radii $\gtrsim 100$ – 200 kpc. In contrast *Chandra*'s excellent spatial resolution ($\sim 0.5''$, corresponding to scales of $\lesssim 2$ kpc even at redshifts as high as ~ 0.2), but modest field of view ($\lesssim 4'$ radius on any single CCD) allows ellipticities to be measured from scales ranging from ~ 1 to ~ 100 kpc. We did not use the *ROSAT* HRI due to its smaller field of view and lower sensitivity than the PSPC.

To define a sample of relaxed clusters we selected the 10 clusters from the PSPC sample of Buote & Tsai (1996) which had the lowest P_3/P_0 ratio within an aperture of $500h_{80}^{-1}$ kpc. We adopted the P_3/P_0 ratio since it is sensitive to unequal-sized mergers (Buote & Tsai 1995), and therefore allows us to eliminate obviously disturbed objects. Although there is evidence of correlations between P_3/P_0 and P_2/P_0 (which is sensitive to the cluster ellipticity) for *disturbed systems* (Buote & Tsai 1996), we would expect a relaxed cluster to have $P_3/P_0 \simeq 0$, and so this selection should not bias us towards low-ellipticity (relaxed) clusters. We excluded one cluster, A 2255, since it has a very extended surface brightness profile that implies that it is not in a relaxed state. We also excluded A 1651 since the existing *Chandra* observation is very shal-

low and the cluster is centered close to a chip gap (restricting the range of radii over which the ellipticity can be computed). Although it is difficult to choose relaxed clusters which exactly match the mass distribution of the simulated clusters, to increase the coverage of lower-mass systems we included A 2589, which just missed our P_3/P_0 cut but is nonetheless very relaxed and has a Virial mass $\sim 3 \times 10^{14} M_\odot$ (Zappacosta et al. 2006). The selected objects, along with properties from Buote & Tsai (1996) are shown in Table 1. To ensure a fair comparison, we also examine the P_3/P_0 ratio for the simulated clusters, and find they are in range of $10^{-8} - 10^{-10}$, consistent with those of observations.

3.4.2. Chandra data reduction

Archival observations of the clusters were drawn from the public *Chandra* archive, and the data were reduced and analyzed with the *CIAO* 3.4 and *Heasoft* 5.3.1 software suites, in conjunction with *Chandra* calibration database (*Caldb*) version 3.3.0.1. To ensure up-to-date calibration, all data were reprocessed from the “level 1” events files, following the standard *Chandra* data-reduction threads². We applied the standard correction to take account of the time-dependent gain-drift and, where possible, charge transfer inefficiency, as implemented in the *CIAO* tools. To identify periods of enhanced background (“flaring”), which seriously degrades the signal-to-noise (S/N) we accumulated background light curves for each data set from low surface-brightness regions of the active chips, excluding obvious point-sources. Periods of flaring were identified by eye and excised. The final exposure times are listed in Table 1. For each data set we generated a full resolution image in the energy 0.3–7.0 keV and corresponding exposure map, computed at an energy of 1.7 keV. Based on experience, such a monochromatic exposure-map is sufficient for our present purposes.

Since our adopted procedure to calculate the ellipticity of a cluster involves taking moments of this image, the presence of bright point-sources (most likely AGN) can lead to errors in the computation. It is therefore essential to identify and remove these objects from the image. Point-sources were detected by application of the *CIAO* task *wavdetect*, which was set to search for structure at scales of 1, 2, 4, 8 and 16 pixels, and supplied with the exposure-maps to minimize spurious detections at the image boundaries. The detection threshold was set to 10^{-6} , corresponding to $\lesssim 1$ spurious source detections per cluster. All detected sources were confirmed by visual inspection, and, for each, appropriate elliptical regions containing approximately 99% of its photons were generated. The detection algorithm also generated a “normalized background” image, which is effectively a smoothed, flat-fielded image, having removed the point-sources found by *wavdetect*.

To generate a cleaned image, suitable for the calculation of ellipticities, the data within each of the elliptical point-source regions were replaced with Poisson-deviated noise. For each pixel, the mean of the Poisson deviate was drawn from the corresponding pixel on the normalized background image, taking into account variations in the exposure-map. Provided the detection algorithm accurately characterizes all the point-sources this is a very robust method for source removal. However, *wavdetect* occasionally mis-identifies extended cluster emission as a point-source, or mis-estimates the radius enclosing most of the source photons, and so the

² <http://cxc.harvard.edu/ciao/threads/index.html>

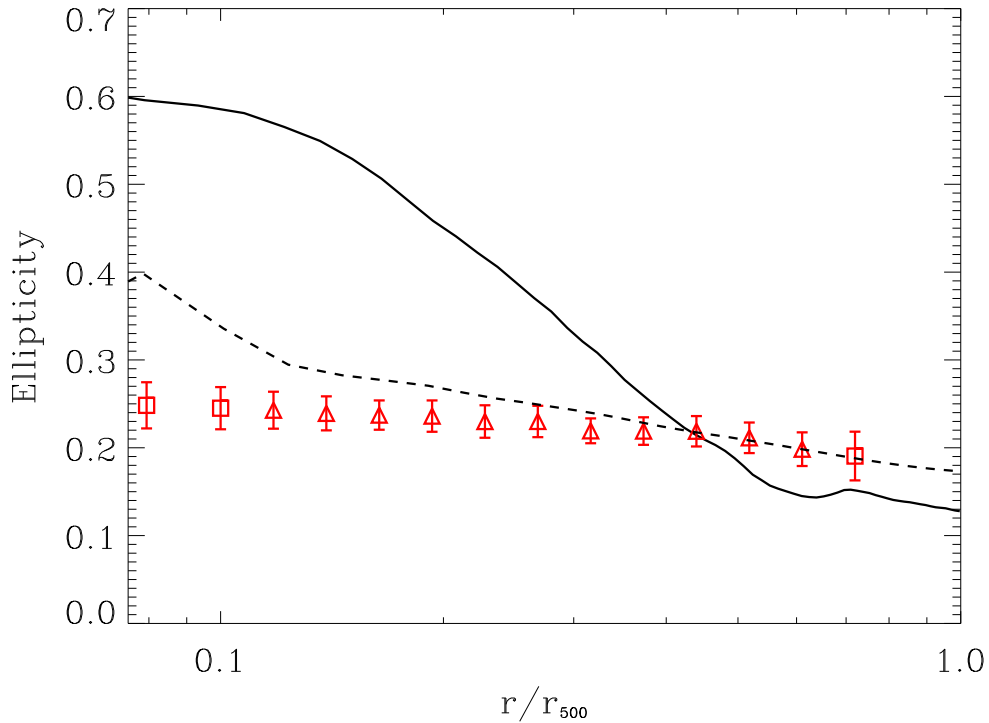


FIG. 8.— Comparison of the average X-ray ellipticity profiles of the “relaxed” simulated CDM clusters (solid black) and the observed clusters (dashed red). For the observed clusters, the inner parts of the ellipticity profile are based on the *Chandra* data, while the outer parts are derived from *ROSAT* PSPC. The error-bars on the observed profile represent the uncertainty on the mean arising from the intrinsic scatter in the measured data. Triangles denote data-points where all 9 observed clusters overlapped, and squares indicate the regions where fewer clusters were used to compute the average profile. Note that none of the observed clusters have ellipticities in excess of ~ 0.3 and none show evidence of profiles which steeply rise towards the center. Dashed line is the ellipticity profile of CL7a from the simulation without radiative cooling or star formation.

background map may be locally incorrect. The point-source free, “cleaned”, image was, therefore, visually inspected to assess how accurately sources were removed. In cases where the source replacement was obviously imperfect, suspicious sources were replaced by assuming the mean (flat-fielded) count-rate per pixel is uniform over the point-source region (this is most correct if the source is at a large radius from the cluster center). This count-rate was estimated for each source by centering a circular extraction region on the source centroid and expanding its radius iteratively until at least 50 photons were found within it, taking care to exclude all photons within any of the source regions. Since the exposure may vary over the pixels within a given source region (especially near the edge of the image), the exposure-map was used to correct this rate on a pixel-by-pixel basis before Poisson noise was added. The final “cleaned” images were visually inspected to confirm reliable source removal. Provided the brightest of the point-sources in an image are removed in this way, any residual (unidentified) sources should not significantly bias our results (Buote & Tsai 1995). Finally, for the computation of the ellipticity profiles, we flattened the image by dividing it by its exposure-map. To confirm the accuracy of the exposure correction, we visually inspected each image (having first mildly smoothed it with a $\sim 10''$ Gaussian filter to aid the eye) for obvious signs of poor flat-fielding. In general, away from the gaps between CCDs, the exposure correction appeared reliable.

3.4.3. ROSAT data reduction

We obtained RDF data for each cluster from the *HEASARC*³ archive, which were reduced and processed with *Heasoft* 5.3.1 and CIAO 3.3.0.1. The data were initially screened to remove (probably spurious) bursts of events with the *burst* task. To ensure conservative screening criteria, we generated a PSPC “makefilter file” using the *pcfilt* task, and screened out events corresponding to a master veto rate in excess of 170 s^{-1} . A light curve was generated from outer parts of the field of view, chosen to avoid obvious bright point-like or extended sources, and was examined by eye to identify periods of enhanced background. Any data taken during such “flares” were excluded from further analysis. Full field of view images were generated in the 0.4–2.0 keV band, with a pixel-size of $15''$, and corresponding exposure maps were generated with the *pcexppmap* task. In addition, a circular cut-out region, centered on the peak of the cluster emission and extending as far as the shadow of the inner PSPC support ring, was created using the *dmcopy* task for both the image and exposure-map. Such a cut prevents the support structure shadows (which are not perfectly removed during flat-fielding) from compromising the calculation of the ellipticities. For those objects with multiple pointings (Table 1), the images and exposure-maps were summed to produce a single “merged” image and exposure-map, using custom software. Before addition, each image was aligned with the image having the longest exposure by shifting it an integer number of pixels in the x and y directions.

Point-sources were detected in the merged cut-out image

³ <ftp://legacy.gsfc.nasa.gov>

TABLE 1
THE CLUSTER SAMPLE

Cluster	Redshift	r_{500} (kpc)	P_2/P_0	P_3/P_0	ObsID	<i>Chandra</i> Exposure (ks)	R_{max} (kpc)	<i>ROSAT</i> ObsID	Exposure (ks)
A2589	0.041	820 ^a	$(2.6^{+0.8}_{-1.0}) \times 10^{-6}$	$(1.1^{+5.9}_{-0.9}) \times 10^{-8}$	7190	53	250	800526	5.9
A2597	0.085	900 ^b	$(1.0^{+0.3}_{-0.4}) \times 10^{-6}$	$(1.6^{+3.1}_{-1.2}) \times 10^{-9}$	7329	58	320	800112	6.2
A2199	0.030	990 ^c	$(5.9 \pm 1.00) \times 10^{-7}$	$(5.1^{+1.2}_{-3.5}) \times 10^{-9}$	497	18	310	150083,800644	43.
MKW3s	0.043	1200 ^a	$(1.6^{+0.5}_{-0.6}) \times 10^{-6}$	$(5.3^{+3.3}_{-4.4}) \times 10^{-9}$	900	57	230	800128	7.5
A1795	0.062	1240 ^d	$(1.3 \pm 0.1) \times 10^{-6}$	$(3.0^{+2.5}_{-3.8}) \times 10^{-10}$	5287	14	310	800055,800105	54.
A2052	0.035	1290 ^a	$(1.3 \pm 0.4) \times 10^{-6}$	$(3.3^{+2.6}_{-2.7}) \times 10^{-9}$	5807	130	290	800275(a01,n00)	6.7
A1413	0.14	1300 ^d	$(5.2^{+2.3}_{-1.7}) \times 10^{-6}$	$(2.2^{+1.0}_{-1.3}) \times 10^{-9}$	5003	75	270	800183	6.4
A2029	0.077	1360 ^d	$(1.4 \pm 0.3) \times 10^{-6}$	$(3.1^{+6.7}_{-2.6}) \times 10^{-9}$	4977	77	300	800161,800249	12.
HydraA	0.052	1390 ^a	$(4.9 \pm 1.3) \times 10^{-7}$	$(4.4^{+10.0}_{-3.6}) \times 10^{-9}$	4969	86	260	800318	16.

NOTE. — The sample of “relaxed” galaxy clusters, sorted in order of increasing P_3/P_0 ratio, as obtained from Buote & Tsai (1995). Also shown are the cluster redshift, the mean cluster temperature (kT), the P_2/P_0 and P_3/P_0 ratios from Buote & Tsai (1996), the observation numbers (“ObsID”) of each *ROSAT* PSPC and *Chandra* data set used in the present paper, and the total cleaned exposure time, following background screening (“Exposure”). For the *Chandra* data, we also indicate the maximum radius to which the data was used in computing the ellipticity profile (R_{max})

r_{500} taken from: ^aFinoguenov et al. (2001), ^bPointecouteau et al. (2005), ^cSanderson et al. (2006), ^dVikhlinin et al. (2006), ^eZappacosta et al. (2006)

with the *wavdetect* algorithm, which was set to search for structure at scales of 1, 2, 4 and 8 pixels, and supplied with the exposure-maps to minimize spurious detections at the image boundaries. The detection threshold was set to 10^{-6} , corresponding to $\lesssim 0.1$ spurious source detections per image. After visual confirmation of the detected sources, the images were “cleaned” of point-sources and flat-fielded, in exactly the same manner as the *Chandra* data. To prevent over-correction during flat-fielding (particularly in areas where the exposure-correction may be questionable), we reset to zero any pixel for which the exposure map fell below 30% of its peak value, and reset the maximum radius inside which the ellipticity can be computed so as not to contain any such pixels.

3.4.4. Ellipticity Profiles

To compute the ellipticity profiles, we adopted a moment-based method that was first developed by Carter & Metcalfe (1980) and later was implemented in the study of the *ROSAT* and *Chandra* image of NGC 720 (see, e.g., Buote & Canizares 1994; Buote et al. 2002) and a sample of five *ROSAT* clusters (Buote & Canizares 1996). In this method, the two-dimensional principal moments of inertia are computed within an elliptical region. The ellipticity, ϵ , is defined as the square root of the ratio of the principal moments. We refer the readers to Buote & Canizares (1994) and Buote et al. (2002) for details.

For each cluster we visually inspected the *Chandra* image for evidence of disturbances in the core, such as bubbles, shocks or cavities, which are most likely a consequence of AGN activity (Bîrzan et al. 2004; Forman et al. 2005; Fabian et al. 2006). Such effects will distort the ellipticity profile computed within the disturbed region but, crucially, the physics of these interactions is not captured by the simulations. Therefore, for each cluster, we estimated the extent of the disturbed region and ignored the ellipticity profile computed within this radius. The moment method we adopted to compute the profile does incorporate information from the pixels in the suspect region. However, the ellipticity is strongly biased towards pixels at large radius and so the method should still yield reliable results. The *Chandra* profiles were computed to as large a radius as possible before a circular aperture of that radius would come in contact with a chip gap or, alternatively, the error-bars on the profile became

large. The maximum extent of each *Chandra* profile is given in Table 1. Outside this radius, the ellipticity data-points were taken from the *ROSAT* data, for which the profile was computed until the edge of the “cut-out” image. In general, we found that the *ROSAT* and *Chandra* profiles matched up well.

In Table 2 we list the observed ellipticity profiles derived for each of the clusters in our sample. In general, the profiles are relatively flat, with a peak ellipticity of ~ 0.2 – 0.3 . We do not find any evidence of sharply rising profiles.

3.5. Comparison of Observed and Simulated CDM Clusters

We show the average X-ray ellipticity profiles of the observed clusters and the simulated CDM clusters ($M > 10^{14} h^{-1} M_{\odot}$) in Fig 8, with 1σ statistical errors on the mean observed values. We also list the average observed ellipticities and their errors in the last column of Table 2. The differences between the profiles are very striking. While the observed clusters have a nearly constant ellipticity profile (~ 0.15), the simulated CSF clusters have much larger ellipticity values (~ 0.3 – 0.6) at small radii (0.1 – $0.4 r_{500}$) before declining to ~ 0.15 near r_{500} . For radii above $\approx 0.6 r_{500}$ both the shape and normalization of the profiles are similar for both the simulated and observed clusters. However, the ellipticity profile of the NC cluster CL7a shows much better agreement with the observed clusters over all radii examined. The relatively small deviations of this single cluster (formed in the simulation without cooling or star formation) from the average ellipticity profile of the observed clusters is consistent with the stochastic variation between the observed clusters (see Table A2).

The pronounced discrepancy over 0.1 – $0.4 r_{500}$, taken together with the discussion in §3.2, demonstrates clearly that the ICM in the simulated clusters rotates much more rapidly than in the observed clusters. Furthermore, this excess ICM rotation in the simulated CDM clusters extends out to $\approx 0.6 r_{500}$ since that is where the ellipticity profiles of the observed and simulated clusters diverge. The averaged profiles for the CSF clusters also are slightly lower than the observations at $> 0.6 r_{500}$, indicating either that the CSF clusters may rotate a little slower than the observed clusters at larger radii and, perhaps more likely, the CSF clusters are slightly more centrally concentrated.

4. DISCUSSION AND CONCLUSION

Over the past decade theoretical studies of cosmological hydrodynamical simulations have emphasized the important role of random turbulent motions in providing pressure support of the ICM in galaxy clusters. Using the set of high-resolution CDM simulations of Nagai et al. (2007) we have shown instead that rotational support of the cluster weight exceeds that of random turbulence from $0.1 - 0.5 r_{500}$ and remains comparable out to $\approx 0.8 r_{500}$ for the clusters classified as the most relaxed in the simulations.

When we compared the average ellipticity profile of the relaxed CDM clusters to that obtained for a set of 9 real nearby clusters observed by *Chandra* and *ROSAT*, we found the simulated CDM clusters are significantly flatter within $\approx 0.4 r_{500}$ and the profile shapes differ interior to $\approx 0.6 r_{500}$. By comparing simulations with and without radiative cooling and star formation, we conclude that this flatness is mainly caused by gas over-cooling and large-scale rotation.

The substantial ICM rotation present in the relaxed simulated CDM clusters very likely indicates that a classical “rotating cooling flow” (Nulsen, Stewart, & Fabian 1984; Kley & Mathews 1994; Brighenti & Mathews 1996) operates in those systems, implying large mass deposition rates which are not observed. At very small radii ($< 0.1 r_{500}$) it is well-known that cosmological hydrodynamical simulations fail to reproduce observed ICM properties because of over-cooling, but since the ICM rotation we have discussed extends to much larger radii, the over-cooling problem apparently does as well.

We stress that the Nagai et al. (2007) simulations are not unusual in regards to displaying signatures of ICM rotation. Recently, Jeltema et al. (2008) compare X-ray images of simulated and observed clusters using power ratios (Buote & Tsai 1995). They find that P_2/P_0 , which is similar to ellipticity, computed within a 0.5 Mpc aperture for their relaxed simulated CDM clusters is slightly larger than for the observed clusters. They also find that distribution of P_3/P_0 , which is

sensitive to asymmetry but not ellipticity, is consistent for the simulated and observed clusters, implying that it is very unlikely that the P_2/P_0 (and hence ellipticity) discrepancy can be attributed to the chosen cosmology. Since 0.5 Mpc corresponds roughly to $0.5 r_{500}$ for clusters, the relatively weak discrepancy is consistent with our results (see Figure 8).

Because the unphysical ICM rotation in the relaxed CDM clusters extends out to a large radius ($\approx 0.6 r_{500}$), ICM quantities determined within these regions in the simulations need to be reconsidered. For example, it has been noted by several authors that X-ray measurements of $M(< r_{500})$ for relaxed clusters assuming hydrostatic equilibrium underestimate the actual mass by 5–20% (e.g., Rasia et al. 2006; Nagai et al. 2007; Burns et al. 2007). But since the X-ray analysis involves fitting gas density and temperature profiles of the ICM over a large radial range interior to r_{500} , the region of unphysical ICM rotation is included in the analysis. (Note that excluding large radial regions can strongly bias X-ray mass estimates – Gastaldello et al. 2007.) While we do not expect these X-ray mass underestimates to change radically for relaxed simulated CDM clusters without unphysical ICM rotation, given that $M_{rot} \sim M_{turb}$ out to $\approx 0.8 r_{500}$ in the simulated clusters we have studied, it is not unreasonable to expect the mass underestimate to be cut in half (see Section 2.4). This would be of considerable importance to studies using X-ray determinations of cluster masses for precision cosmology.

Acknowledgments: We thank Daisuke Nagai for providing the sample of simulated clusters and a careful reading of our manuscript. We also thank the referee for helpful comments. We thank Renyue Cen, Fabio Gastaldello, Andrey Kravtsov, Luca Zappacosta for helpful discussions. We gratefully acknowledge partial support from NASA through *Chandra* Award Number GO6-7118X, GO6-7120X, GO6-7671X, and NNG04GE76G, issued through the Office of Space Sciences Long-Term Space Astrophysics Program.

REFERENCES

- Allen, S. W., Rapetti, D. A., Schmidt, R. W., Ebeling, H., Morris, R. G., Fabian, A. C. 2007, MNRAS, in press (arXiv:0706.0033)
- Bîrzan, L., Rafferty, D. A., McNamara, B. R., Wise, M. W., & Nulsen, P. E. J. 2004, ApJ, 607, 800
- Binney, J., & Tremaine, S. 1987, Princeton, NJ, Princeton University Press, 1987
- Brighenti, F., & Mathews, W. G. 1996, ApJ, 470, 747
- Brîggen, M., Hoeft, M., & Ruszkowski, M. 2005, ApJ, 628, 153
- Brunetti, G., & Lazarian, A. 2007, MNRAS, 378, 245
- Buote, D. A., Gastaldello, F., Humphrey, P. J., Zappacosta, L., Bullock, J. S., Brighenti, F., & Mathews, W. G. 2007, ApJ, 664, 123
- Buote, D. A., Jeltema, T. E., Canizares, C. R., & Garmire, G. P. 2002, ApJ, 577, 183
- Buote, D. A., & Canizares, C. R. 1998, MNRAS, 298, 811
- Buote, D. A., & Canizares, C. R. 1996, ApJ, 457, 565
- Buote, D. A., & Canizares, C. R. 1994, ApJ, 427, 86
- Buote, D. A., & Tsai, J. C. 1996, ApJ, 458, 27
- Buote, D. A., & Tsai, J. C. 1995, ApJ, 452, 522
- Burns, J. O., Hallman, E. J., Gantner, B., Motl, P. M., & Norman, M. L. 2007, ArXiv e-prints, 708, arXiv:0708.1954
- Carter, D., & Metcalfe, N. 1980, MNRAS, 191, 325
- Chepurnov, A., & Lazarian, A. 2006, ArXiv Astrophysics e-prints, arXiv:astro-ph/0611463
- David, L. P., Nulsen, P. E. J., McNamara, B. R., Forman, W., Jones, C., Ponman, T., Robertson, B., & Wise, M. 2001, ApJ, 557, 546
- Dolag, K., Vazza, F., Brunetti, G., & Tormen, G. 2005, MNRAS, 364, 753
- Dupke, R. A., & Bregman, J. N. 2006, ApJ, 639, 781
- Evrard, A. E., Metzler, C. A., & Navarro, J. F. 1996, ApJ, 469, 494
- Fabian, A. C., Sanders, J. S., Taylor, G. B., Allen, S. W., Crawford, C. S., Johnstone, R. M., & Iwasawa, K. 2006, MNRAS, 366, 417
- Faltenbacher, A., Kravtsov, A. V., Nagai, D., & Gottl ber, S. 2005, MNRAS, 358, 139
- Finoguenov, A., Arnaud, M., & David, L. P. 2001, ApJ, 555, 191
- Forman, W., et al. 2005, ApJ, 635, 894
- Gastaldello, F., Buote, D. A., Humphrey, P. J., Zappacosta, L., Bullock, J. S., Brighenti, F., & Mathews, W. G. 2007, ApJ, 669, 158
- Hallman, E. J., Motl, P. M., Burns, J. O., & Norman, M. L. 2006, ApJ, 648, 852
- Inogamov, N. A., & Sunyaev, R. A. 2003, Astronomy Letters, 29, 791
- Jeltema, T. E., Hallman, E. J., Burns, J. O., & Motl, P. M. 2008, ApJ, 681, 167
- Kay, S. T., Thomas, P. A., Jenkins, A., & Pearce, F. R. 2004, MNRAS, 355, 1091
- Kley, W., & Mathews, W. G. 1995, ApJ, 438, 100
- Klypin, A., Kravtsov, A. V., Bullock, J. S., & Primack, J. R. 2001, ApJ, 554, 903
- Kravtsov, A. V., Vikhlinin, A., & Nagai, D. 2006, ApJ, 650, 128
- Kravtsov, A. V., Klypin, A., & Hoffman, Y. 2002, ApJ, 571, 563
- Lau, E. 2008, in preparation
- Lewis, A. D., Buote, D. A., & Stocke, J. T. 2003, ApJ, 586, 135
- Mathews, W. G., & Brighenti, F. 2003, ARA&A, 41, 191
- Nagai, D., Vikhlinin, A., & Kravtsov, A. V. 2007, ApJ, 655, 98
- Nulsen, P. E. J., Stewart, G. C., & Fabian, A. C. 1984, MNRAS, 208, 185
- Pawl, A., Evrard, A. E., & Dupke, R. A. 2005, ApJ, 631, 773
- Pointecouteau, E., Arnaud, M., & Pratt, G. W. 2005, A&A, 435, 1
- Pratt, G. W., & Arnaud, M. 2003, A&A, 408, 1
- Rasia, E., et al. 2006, MNRAS, 369, 2013
- Rasia, E., Tormen, G., & Moscardini, L. 2004, MNRAS, 351, 237
- Sanderson, A. J. R., Ponman, T. J., & O’Sullivan, E. 2006, MNRAS, 372, 1496
- Schuecker, P., Finoguenov, A., Miniati, F., B hringer, H., & Briel, U. G. 2004, A&A, 426, 387
- Stanek, R., Evrard, A. E., B hringer, H., Schuecker, P., & Nord, B. 2006, ApJ, 648, 956
- Sunyaev, R. A., Norman, M. L., & Bryan, G. L. 2003, Astronomy Letters, 29, 783

- Thomas, P. A., et al. 1998, MNRAS, 296, 1061
 Tsai, J. C., Katz, N., & Bertschinger, E. 1994, ApJ, 423, 553
 Vazza, F., Tormen, G., Cassano, R., Brunetti, G., & Dolag, K. 2006, MNRAS, 369, L14
 Vikhlinin, A., Kravtsov, A., Forman, W., Jones, C., Markevitch, M., Murray, S. S., & Van Speybroeck, L. 2006, ApJ, 640, 691
 Vikhlinin, A., Markevitch, M., Murray, S. S., Jones, C., Forman, W., & Van Speybroeck, L. 2005, ApJ, 628, 655
 Zappacosta, L., Buote, D. A., Gastaldello, F., Humphrey, P. J., Bullock, J., Brighenti, F., & Mathews, W. 2006, ApJ, 650, 777

APPENDIX

OBSERVED CLUSTER ELLIPTICITY PROFILES

We show in Table 2 the observed ellipticity profiles of each of the clusters considered in § 3.4.4.

TABLE 2
OBSERVED CLUSTER ELLIPTICITY PROFILES

r/r ₅₀₀	Observed cluster									
	A2589	A2597	A2199	MKW3s	A1795	A2052	A1413	A2029	HydraA	Average
0.010	0.090 ± 0.031
0.013	0.14 ± 0.03
0.016	0.16 ± 0.02
0.020	0.20 ± 0.01
0.025	0.198 ± 0.010
0.032	0.17 ± 0.05	0.235 ± 0.008
0.040	0.26 ± 0.03	0.252 ± 0.007
0.050	0.31 ± 0.03	0.262 ± 0.005
0.063	0.31 ± 0.03	...	0.179 ± 0.005	0.226 ± 0.006	0.250 ± 0.006	...	0.34 ± 0.01	0.258 ± 0.004
0.079	0.31 ± 0.02	...	0.192 ± 0.005	0.268 ± 0.005	0.267 ± 0.007	0.201 ± 0.002	0.369 ± 0.009	0.254 ± 0.004	0.128 ± 0.002	0.248 ± 0.026
0.10	0.314 ± 0.010	...	0.204 ± 0.004	0.26 ± 0.03	0.272 ± 0.006	0.15 ± 0.02	0.344 ± 0.009	0.248 ± 0.003	0.166 ± 0.002	0.245 ± 0.024
0.12	0.314 ± 0.008	0.188 ± 0.003	0.197 ± 0.009	0.31 ± 0.02	0.261 ± 0.007	0.18 ± 0.02	0.321 ± 0.007	0.249 ± 0.002	0.166 ± 0.002	0.243 ± 0.021
0.14	0.31 ± 0.02	0.198 ± 0.003	0.208 ± 0.006	0.29 ± 0.02	0.250 ± 0.006	0.16 ± 0.02	0.319 ± 0.007	0.255 ± 0.002	0.170 ± 0.009	0.239 ± 0.019
0.16	0.28 ± 0.05	0.202 ± 0.005	0.200 ± 0.005	0.27 ± 0.03	0.250 ± 0.006	0.18 ± 0.02	0.317 ± 0.007	0.259 ± 0.002	0.18 ± 0.01	0.237 ± 0.017
0.19	0.29 ± 0.04	0.203 ± 0.004	0.192 ± 0.006	0.27 ± 0.02	0.243 ± 0.008	0.17 ± 0.02	0.327 ± 0.006	0.26 ± 0.01	0.18 ± 0.01	0.236 ± 0.018
0.23	0.26 ± 0.03	0.210 ± 0.002	0.186 ± 0.005	0.24 ± 0.02	0.245 ± 0.004	0.18 ± 0.01	0.338 ± 0.006	0.258 ± 0.008	0.154 ± 0.009	0.230 ± 0.018
0.27	0.26 ± 0.03	0.202 ± 0.004	0.184 ± 0.005	0.24 ± 0.02	0.237 ± 0.004	0.21 ± 0.01	0.339 ± 0.004	0.25 ± 0.01	0.152 ± 0.008	0.230 ± 0.017
0.32	0.25 ± 0.03	0.20 ± 0.01	0.170 ± 0.003	0.24 ± 0.02	0.225 ± 0.004	0.21 ± 0.01	0.28 ± 0.03	0.248 ± 0.008	0.149 ± 0.008	0.219 ± 0.014
0.37	0.25 ± 0.03	0.22 ± 0.02	0.176 ± 0.003	0.26 ± 0.02	0.213 ± 0.004	0.20 ± 0.01	0.29 ± 0.03	0.22 ± 0.01	0.137 ± 0.009	0.219 ± 0.016
0.44	0.26 ± 0.03	0.22 ± 0.02	0.169 ± 0.003	0.28 ± 0.02	0.200 ± 0.003	0.21 ± 0.01	0.29 ± 0.03	0.201 ± 0.009	0.14 ± 0.01	0.219 ± 0.017
0.52	0.26 ± 0.02	0.20 ± 0.02	0.150 ± 0.004	0.23 ± 0.03	0.191 ± 0.003	0.25 ± 0.02	0.29 ± 0.03	0.187 ± 0.008	0.136 ± 0.007	0.211 ± 0.017
0.61	0.28 ± 0.02	0.22 ± 0.01	0.138 ± 0.004	0.15 ± 0.04	0.180 ± 0.006	0.21 ± 0.02	0.30 ± 0.03	0.17 ± 0.01	0.146 ± 0.009	0.198 ± 0.019
0.72	0.27 ± 0.02	0.23 ± 0.02	...	0.082 ± 0.045	0.154 ± 0.004	...	0.28 ± 0.03	0.132 ± 0.008	0.19 ± 0.01	0.190 ± 0.028
0.85	0.25 ± 0.02	0.24 ± 0.03	0.31 ± 0.03	0.12 ± 0.01
1.0	...	0.20 ± 0.03	0.25 ± 0.04